Direct numerical simulations of dynamic gas-solid suspensions

Direct Numerical Simulations of Dynamic Gas-Solid Suspensions

Yali Tang, E. A. J. F. Peters, and J. A. M. Kuipers
Dept. of Chemical Engineering and Chemistry, Multiphase Reactors Group, Eindhoven University of Technology, P.O. Box 513, 5600, MB Eindhoven, The Netherlands

DOI 10.1002/aic.15197
Published online February 18, 2016 in Wiley Online Library (wileyonlinelibrary.com)

Direct numerical simulation results for gas flow through dynamic suspensions of spherical particles is reported. The simulations are performed using an immersed boundary method, with careful correction for the grid resolution effect. The flow systems we have studied vary with mean flow Reynolds number, solids volume fraction, as well as particle/gas density ratio. On the basis of the simulation results, the effect of particle mobility on the gas-solid drag force is analyzed and introduced into the existing drag correlation that was derived from simulations of stationary particles. This mobility effect is characterized by the granular temperature, which is a result of the particle velocity fluctuation. The modified drag correlation is considered so-far the most accurate expression for the interphase momentum exchange in computational fluid dynamics models, in which the gas-solid interactions are not directly resolved. © 2016 American Institute of Chemical Engineers *AIChE J*, 62: 1958–1969, 2016
Keywords: direct numerical simulation, drag correlation, moving particles

Introduction

Gas-solid flows are characterized by the presence of solid particles in a gas phase and are commonly encountered in nature, as well as industrial applications such as energy generation, food production, pharmaceutical processing, and so on. For the efficiency of such processes, the solids and gas phases usually need to be brought into intimate contact. A widely used type of process reactors for thorough gas-solid contacting is gas-fluidized beds. Quantitative understanding of gas-solid flows is crucial for effective operations and optimization of processes involving fluidized beds. In this respect, computational fluid dynamics (CFD) simulations can, in many cases, complement experimental studies by providing detailed information that is difficult to obtain otherwise. The numerical prediction of fluidized bed behavior in engineering scale equipment can, in practice, only be achieved with continuum models such as the two-fluid model (TFM).[1–5] Such simulations are typically based on averaged equations of mass and momentum conservation corresponding for both phases. In recent years, discrete element methods combined with a continuum approach for the gas phase (CFD-DEM) have also become increasingly popular for modeling gas-solid flows.[6–10] In this model, the solid phase is described in a discrete fashion, where the Newtonian equations of motion for each particle are solved. For the gas phase, an averaged equation of motion is solved just like in the TFM. A common feature of these models is that the flow between particles is not resolved, which leads to a term in the momentum conservation equation representing the average interphase momentum transfer between the gas and particles. This term is typically referred to as the drag correlation, which depends on averaged flow quantities such as the Reynolds number (Re) based on mean superficial velocity, solids volume fraction (ϕ), particle-size distribution, and so on. An accurate drag correlation for the representation of the gas-solid momentum transfer is essential to perform predictive coarse-grained CFD simulations, which is, however, one of the biggest challenges in the community of multiphase flows.

Direct numerical simulation (DNS) is based on a first-principles approach that can provide insight and data to develop accurate models for interphase momentum exchange in gas-solid flows. DNS treats the gas-particle interactions *ab initio* with exact boundary conditions imposed at the surface of individual particles, such that the flow between particles is resolved. There are different numerical approaches available to perform DNS of gas-solid flows, which can be broadly classified as those that rely on a body-fitted mesh[11–15] to impose boundary conditions at particle surfaces and those that use regular Cartesian grids.[16–23] The principle disadvantage of the body-fitted methods is that repeated re-meshing and solution projection are required for moving particles. These needs are eliminated for methods that employ regular Cartesian grids, resulting in a much faster solution process for moving particles. Moreover, the need to perform multiple independent simulations due to the wide range of parameters encountered in gas-solid flows makes it practical to use regular meshes, even for fixed particles. Note that because the grid does not conform to the particle surface, special attention is needed to generate an accurate solution by imposing boundary conditions at the particle surface, see a detailed description in Tenneti et al.[24] An authoritative compendium of particle-resolved

Correspondence concerning this article should be addressed to E. A. J. F. Peters at E.A.J.F.Peters@tue.nl.

DNS approaches for a wide class of multiphase flows can be found in Prosperetti and Tryggvason.[25] For a recent overview on DNS of mass momentum and heat transport in dense gas-solid flows see Deen et al.[26]

To develop a drag closure, it is natural to perform DNSs of a statistically homogeneous suspension flow with freely moving particles over a wide range of flow quantities (like Re and ϕ), which were, however, computationally prohibitive in the past. A general simplification for high Stokes number particles (such as in gas fluidization) is to simulate steady flow past assemblies of stationary particles with sampled configurations, where ultimately the drag force is obtained by averaging over these samples. This idea has been exploited to extract drag correlations by several researchers. For example, Hill et al.[27,28] proposed a drag correlation based on the Lattice Boltzmann Method (LBM) simulations of steady flow past both ordered and random arrays of stationary spheres. van der Hoef et al.[29] and Beetstra et al.[30] obtained the drag correlation by extending such LBM simulations to mono- and bidisperse arrays of fixed spheres at low and intermediate Reynolds numbers. Tenneti et al.[31] studied flow past static random assemblies of monodisperse spheres using a Particle-resolved Uncontaminated-fluid Reconcilable Immersed Boundary Method and proposed a new drag correlation. In our previous study,[32] we obtained a drag correlation on the basis of highly accurate data obtained from Immersed Boundary Method (IBM) simulations of stationary particles, which extend all earlier reported studies to a wider range of ϕ and Re.

Despite such extensive studies of stationary particles, dynamic particles are more realistic and are in principle preferred for developing closures required in predictive coarse-grained CFD models of gas-fluidized beds. This insight drives increasing attention and effort on DNSs of moving particles,[33–37] which are, however, much more complex compared to stationary particles. An increase of the gas–solid interaction force associated with the granular temperature (energy contained in the particle velocity fluctuations) was reported by Wylie et al.[38] and Tenneti et al.,[39] based on DNS of flows past homogeneous suspensions of monodisperse particles possessing random motion in a periodic box. Yin and Sundaresan[40] performed LBM simulations of low-Re flow in bidisperse fixed beds and suspensions with particle-particle relative motions. Comparison of their simulation results indicated that the particle-particle momentum transfer in freely evolving suspensions is an important contribution to the fluid-particle drag in such systems. Recently, DNS of a small fluidized bed consisting of 2000 particles was performed by Kriebitzsch et al.[41] and compared to CFD-DEM simulation results of exactly the same system. It was found that the (true) DNS force is significantly larger than the gas-solid force computed in CFD-DEM simulations via existing well-accepted drag correlations that were obtained for stationary particles, as typically implemented in current CFD-DEM and TFM models. The conclusion was drawn that the application of existing *static* drag correlations for gas-solid systems with particle granular temperature (such as in fluidized beds) is a crude approximation. Therefore, to obtain a more accurate description of the hydrodynamic force in gas-fluidized systems, the effect of the local relative motion (granular temperature) of the particles should be considered in the drag representation.

In this work, DNS of dynamic gas-solid suspensions was performed using the IBM for wide ranges of flow quantities such as Re, ϕ and particle/gas density ratio ρ_p/ρ_g. The computed drag force is compared with those for stationary particles from our earlier work,[32] consequently the effect of particle mobility on the drag force is quantified. Subsequently, a modified drag correlation including this mobility effect is obtained, which can better represent the gas-solid interactions in larger-scale CFD simulations of gas-solid flows as encountered in gas-fluidized beds. This article is organized in the following way: The numerical method for DNS of gas-solid flows is first introduced, followed by a validation of this method for modeling a single sphere sedimentation; Subsequently, in the results section the granular temperature and the drag force in flows past freely moving spheres are reported, as well as a modified *dynamic* drag correlation; Finally, conclusions are drawn at the end of this article.

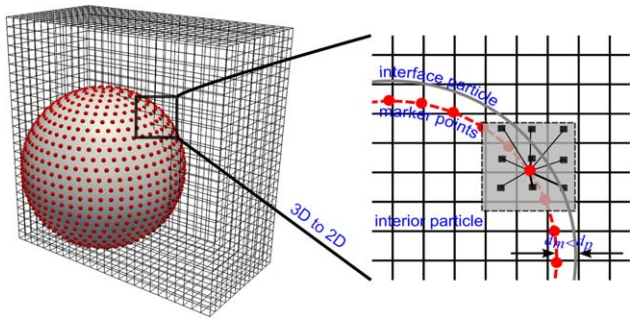

Figure 1. Schematic explanation of the IBM: representation of an immersed particle on a Cartesian grid by a set of marker points (left), the interpolation, and extrapolation of quantities between a marker point and grid points (right).

[Color figure can be viewed in the online issue, which is available at wileyonlinelibrary.com.]

Numerical Method

The problem considered in this work is a system of spherical particles immersed in the flow of an incompressible Newtonian fluid, with constant physical properties. An immersed boundary method is adopted to perform DNS of such a system. A schematic explanation of this method is given in Figure 1, and additional information is given below.

Gas phase equations

The transport phenomena in the gas phase are governed by the conservation equations for mass (Eq. 1) and momentum (Eq. 2), which are solved in three dimensions on a fixed and structured Cartesian grid with the grid spacing h much smaller than the particle diameter d_p

$$\nabla \cdot \mathbf{u} = 0 \tag{1}$$

$$\rho_g \frac{\partial \mathbf{u}}{\partial t} + \rho_g(\nabla \cdot \mathbf{uu}) = -\nabla P + \mu_g \nabla^2 \mathbf{u} + \mathbf{f}^{IB} \tag{2}$$

where ρ_g, μ_g, $\mathbf{u}$, and P represent the density, viscosity, velocity, and modified pressure ($P = p - \rho_g \mathbf{g} \cdot \mathbf{x}$) of the gas, respectively. The forcing term $\mathbf{f}^{IB}$ in Eq. 2 is the external force exerted on the flow field due to the presence of the immersed particles. The calculation of this force density constitutes a key aspect of the IB techniques, and will be described later.

Standard central second-order finite differences are used to discretize Eq. 1 together with Eq. 2 in space, except for the convective terms that are discretized by a second-order flux-

limited Barton-scheme.[42] For the temporal discretization of the momentum equations, the explicit second-order Adams-Bashforth scheme is used for the convective terms, whereas the Crank–Nicholson scheme is used for the viscous term. We use a robust and very efficient Incomplete-Cholesky-Conjugate-Gradient algorithm to solve the resulting sparse matrix equation for each velocity component. It should be stressed here that the flow field is solved in the entire computational domain.

Gas-solid coupling

On the surface Γ_i of an immersed particle i, the fluid velocity $\mathbf{u}$ has to satisfy the no-slip boundary condition, meaning that the fluid velocity equals the particle velocity at its surface, which follows as

$$\mathbf{u}(\mathbf{x}) = \mathbf{v}_i + \boldsymbol{\omega}_i \times (\mathbf{x} - \mathbf{r}_i) \quad \forall \mathbf{x} \in \Gamma_i \tag{3}$$

where, $\mathbf{v}_i$ and $\boldsymbol{\omega}_i$ represent the translational and rotational velocity of particle i; $(\mathbf{x} - \mathbf{r}_i)$ is the vector from the particle mass center $\mathbf{r}_i$ to the location $\mathbf{x}$. This condition is fulfilled in an indirect manner by a forcing term $\mathbf{f}^{\mathrm{IB}}$ in the momentum equation Eq. 2.

In the immersed boundary method, each particle is represented by a set of marker points as shown in Figure 1. The locations of marker points usually do not coincide with the Cartesian grid points where the components of the fluid velocity are defined. Thus, a so-called discrete or regularized delta function $D(\mathbf{x} - \mathbf{X})$ is used to transfer information or physical quantities between the marker points $\mathbf{X}_m$ and the Cartesian grid points $\mathbf{x}$. Usually, the three-dimensional (3-D) delta function is simply constructed by the multiplication of one-dimensional delta functions, that is

$$D\left(\frac{\mathbf{x}-\mathbf{X}_m}{h}\right) = \delta\left(\frac{x-X_m}{h}\right) \cdot \delta\left(\frac{y-Y_m}{h}\right) \cdot \delta\left(\frac{z-Z_m}{h}\right) \tag{4}$$

where, a cheap clipped fourth-order polynomial function proposed by Deen et al.[43] is used in this work. With a support of three times the grid size ($s = 1.5h$), their function is written as

$$\delta(x-X) = \begin{cases} \dfrac{15}{16}\left[\dfrac{(x-X)^4}{s^5} - 2\dfrac{(x-X)^2}{s^3} + \dfrac{1}{s}\right] & -s \le (x-X) \le +s, \\ 0 & \text{else} \end{cases} \tag{5}$$

Thus, the velocity $\mathbf{U}_m$ at the marker points is interpolated from the fluid velocity field $\mathbf{u}_{i,j,k}$ via

$$\mathbf{U}_m = \sum_i \sum_j \sum_k D\left(\frac{\mathbf{x}_{i,j,k}-\mathbf{X}_m}{h}\right) \cdot \mathbf{u}_{i,j,k} \tag{6}$$

Subsequently, the Lagrangian IB force at each marker point is calculated according to

$$\mathbf{F}_m^{\mathrm{IB}} = \rho_{\mathrm{g}} \cdot \frac{\mathbf{V}_m - \mathbf{U}_m}{\Delta t} \tag{7}$$

where, $\mathbf{V}_m$ represents the particle velocity at this marker point, which is calculated via the rhs of Eq. 3; Δt represents the time step.

However, the force density $\mathbf{f}^{\mathrm{IB}}$ is needed for Eq. 2 on the Eulerian grids, which requires the following reverse operation by spreading the Lagrangian force $\mathbf{F}_m^{\mathrm{IB}}$ calculated for the marker points to the surrounding grid points

$$\mathbf{f}_{i,j,k}^{\mathrm{IB}} = \sum_m D\left(\frac{\mathbf{x}_{i,j,k}-\mathbf{X}_m}{h}\right) \cdot \mathbf{F}_m^{\mathrm{IB}} \cdot \frac{\Delta V_m}{h^3} \tag{8}$$

with ΔV_m the volume assigned to each marker point.

Solid phase equations

The motion of a rigid particle i is described by Newton's equation of motion, thus the translational velocity $\mathbf{v}_i$ and the rotational velocity $\boldsymbol{\omega}_i$ evolve, respectively, according to

$$\rho_{\mathrm{p},i} V_{\mathrm{p},i} \frac{d\mathbf{v}_i}{dt} = (\rho_{\mathrm{p},i} - \rho_{\mathrm{g}}) V_{\mathrm{p},i} \mathbf{g} + \mathbf{F}_{\mathrm{g}\to s,i} + \sum_{j\neq i} \mathbf{F}_{\mathrm{c},j\to i} \tag{9}$$

$$\Theta_{\mathrm{p},i} \frac{d\boldsymbol{\omega}_i}{dt} = \mathbf{T}_{\mathrm{g}\to s,i} + \sum_{j\neq i} \mathbf{T}_{\mathrm{c},j\to i} \tag{10}$$

where $V_{\mathrm{p},i}$, $\rho_{\mathrm{p},i}$, and $\Theta_{\mathrm{p},i}$ represent the volume, density, and moment of inertia of particle i, respectively; and ρ_{g} is the gas density. The terms on the rhs of Eq. 9 are the gravity reduced by buoyancy, the gas–particle interaction force $\mathbf{F}_{\mathrm{g}\to s,i}$ and the total collision force $\mathbf{F}_{\mathrm{c},j\to i}$ with other particles. While, in Eq. 10 they are the fluid-particle torque $\mathbf{T}_{\mathrm{g}\to s,i}$ and the total collisional torque $\mathbf{T}_{\mathrm{c},j\to i}$. Note that the buoyancy term is not included in an explicit manner in the equation of motion for the particles, since it is accounted for in the calculation of the pressure force acting on the particle surface. For the particle-particle interactions, perfectly elastic collisions are considered in this work using a standard hard-sphere model,[44] which is based on conservation laws for linear and angular momentum. A characteristic feature of a hard-sphere model is that a sequence of binary collisions is processed, one collision at a time, assuming instantaneous collisions. In principle, the gas-particle interactions can be calculated from numerical quadrature of the surface integrals. However, an alternative evaluation of the gas-particle interaction force is employed using the IB force density $\mathbf{f}^{\mathrm{IB}}$ A balance of the linear and angular momentum for the artificial fluid that covers the volume of a particle gives, respectively[18]

$$\frac{d}{dt}\int_{V_{\mathrm{p},i}} \rho_{\mathrm{g}} \mathbf{u} d\Omega = -\oint_{\Gamma_i} (P\mathbf{n} + \mathbf{S}\cdot\mathbf{n}) d\sigma + \int_{V_{\mathrm{p},i}} \mathbf{f}^{\mathrm{IB}} d\Omega \tag{11}$$

$$\begin{aligned} \frac{d}{dt}\int_{V_{\mathrm{p},i}} \rho_{\mathrm{g}} (\mathbf{X}_m - \mathbf{r}_i) \times \mathbf{u} d\Omega = &-\oint_{\Gamma_i} ((\mathbf{x}-\mathbf{r}_i) \times (\mathbf{S}\cdot\mathbf{n})) d\sigma \\ &+ \int_{V_{\mathrm{p},i}} (\mathbf{X}_m - \mathbf{r}_i) \times \mathbf{f}^{\mathrm{IB}} d\Omega \end{aligned} \tag{12}$$

The second terms in Eqs. 11 and 12 are by definition the gas-solid force $\mathbf{F}_{\mathrm{g}\to s,i}$ and torque $\mathbf{T}_{\mathrm{g}\to s,i}$ acting on the particle. The last terms are easily calculated by summation of the force density acting on the marker points. Thus

$$\mathbf{F}_{\mathrm{g}\to s,i} = -\left(\sum_m \mathbf{F}_m^{\mathrm{IB}} \cdot \Delta V_m - \frac{d}{dt}\int_{V_{\mathrm{p},i}} \rho_{\mathrm{g}} \mathbf{u} d\Omega\right) \tag{13}$$

$$\mathbf{T}_{\mathrm{g}\to s,i} = -\left(\sum_m (\mathbf{X}_m - \mathbf{r}_i) \times \mathbf{F}_m^{\mathrm{IB}} \cdot \Delta V_m - \frac{d}{dt}\int_{V_{\mathrm{p},i}} \rho_{\mathrm{g}} (\mathbf{X}_m - \mathbf{r}_i) \times \mathbf{u} d\Omega\right) \tag{14}$$

Note that the inertia of the artificial fluid inside the volume occupied by the particle i also contributes to the IB forcing term, and, therefore, has to be subtracted to obtain the correct interaction force. Moreover, it can be shown[18] that the inertia of the artificial fluid is equal to the change of linear

momentum of the center of mass of the internal fluid inside the particle

$$\frac{d}{dt}\int_{V_{\mathrm{p},i}} \rho_{\mathrm{g}}\mathbf{u}d\Omega = \rho_{\mathrm{g}}V_{\mathrm{p},i}\frac{d\mathbf{v}_i}{dt} \tag{15}$$

$$\frac{d}{dt}\int_{V_{\mathrm{p},i}} \rho_{\mathrm{g}}(\mathbf{X}_m-\mathbf{r}_i)\times\mathbf{u}d\Omega = \frac{\rho_{\mathrm{g}}\Theta_{\mathrm{p},i}}{\rho_{\mathrm{p},i}}\frac{d\boldsymbol{\omega}_i}{dt} \tag{16}$$

Thus, Eqs. 9 and 10 are converted into

$$(\rho_{\mathrm{p},i}-\rho_{\mathrm{g}})V_{\mathrm{p},i}\frac{d\mathbf{v}_i}{dt} = (\rho_{\mathrm{p},i}-\rho_{\mathrm{g}})V_{\mathrm{p},i}\mathbf{g} - \sum_m \mathbf{F}_m^{\mathrm{IB}}\cdot\Delta V_m + \sum_{j\neq i}\mathbf{F}_{\mathrm{c},j\to i} \tag{17}$$

$$(\rho_{\mathrm{p},i}-\rho_{\mathrm{g}})\frac{\Theta_{\mathrm{p},i}}{\rho_{\mathrm{p},i}}\frac{d\boldsymbol{\omega}_i}{dt} = -\sum_m (\mathbf{X}_m-\mathbf{r}_i)\times\mathbf{F}_m^{\mathrm{IB}}\cdot\Delta V_m + \sum_{j\neq i}\mathbf{T}_{\mathrm{c},j\to i} \tag{18}$$

Note that in traditional IBMs, the marker points are specified to be uniformly distributed over the surface of particles. However, as a consequence of the use of a regularized delta function, the sharp interface of the particle is smeared into a thin spherical shell, and the boundary where the no-slip condition is truly fulfilled departs slightly away from the real particle surface. Consequently, the accuracy of such IBM simulations is poor, especially at relatively low resolutions. In contrast, we use an optimal diameter d_m for the marker points distribution according to the methodology detailed in Tang et al.[45] The principle of this methodology is that, by locating the marker points slightly inwards the interior of the particle as shown in Figure 1, the no-slip boundary condition is supposed to be satisfied as close as possible to the particle surface, and consequently the accuracy is improved for predictions of the gas-solid interactions as well as the flow field. The values of the optimal d_m used in the presented simulations are individually evaluated for different solids volume fractions and Reynolds numbers.

Validation of a single sphere sedimentation

Extensive standard validations of this IBM have been given by Kriebitzsch[46] as well as Tang et al.,[45] including Stokes and non-Stokes flows past a single fixed sphere, regular and random arrays of fixed spheres, and the interaction force between two-approaching spheres. As the IBM is applied to simulate dynamic particles in the present work, an additional validation is performed for a single sphere sedimentation in an enclosure.

Table 1. Fluid Densities and Viscosities, as well as Re_{p} for a Single Sphere Sedimentation

	Case 1	Case 2	Case 3	Case 4
ρ_f [kg/m^3]	970	965	962	960
μ_f [kg/(m s)]	0.373	0.212	0.113	0.058
Re_{p} [−]	1.5	4.1	11.6	31.6

We perform the simulations using the experimental set-ups and data as reported in ten Cate et al.[47] A single sphere with a diameter $d_{\mathrm{p}} = 15$ mm and density $\rho_{\mathrm{p}} = 1120$ kg/m^3 is released from its rest position at a height of $H = 120$ mm from the bottom of a box with dimensions $depth \times width \times height = 100 \times 100 \times 160$ mm. Four different fluid properties as listed in Table 1 are considered, corresponding to different Reynolds numbers Re_{p} based on the particle terminal velocity. The free-slip condition is used for the domain boundaries. A grid resolution of $d_{\mathrm{p}}/h = 12$ is used, together with $d_m = 14.2$ mm for the marker point distribution.

In Figure 2, the particle trajectories and settling velocities vs. time are plotted for simulation results as well as the experimental data reported by ten Cate et al.[47] A very good agreement between the simulations and experiments can be observed. This indicates that with the appropriate modification of the marker points distribution, our method produces quite accurate results at a relatively low resolution for systems with moving particles.

Dynamic Gas-Solid Suspensions

IBM simulations of dynamic gas-solid suspensions are conducted in a periodic 3-D domain along with zero initial velocity of the particles. An initial particle configuration is created using a standard hard sphere Monte-Carlo method[48]: all the particles are first placed in an ordered face-centered-cubic configuration; then each particle is randomly moved, with the displacement accepted only if no overlap is detected at the new position with any of the other particles; such a random displacement is iterated till that the particles are randomly distributed in the computational domain. Note that, this hard-

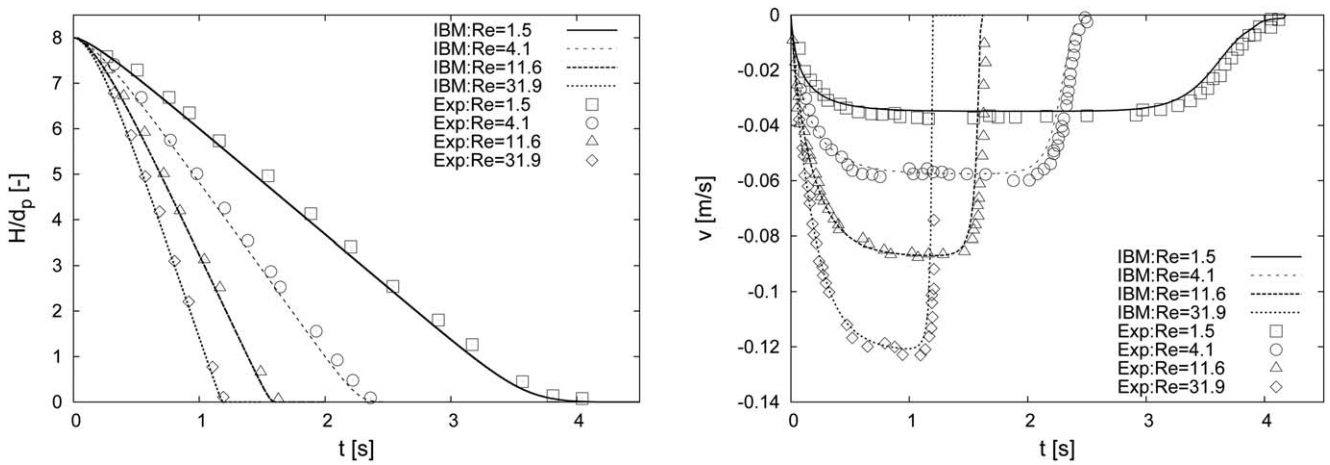

Figure 2. Particle trajectories (left) and sedimentation velocities (right) for a single sphere sedimentation in an enclosure.

Table 2. Simulation Parameters for Investigating the Effect of Domain Size and Viscosity

ϕ	$\frac{\rho_p}{\rho_g}$	$\frac{d_p}{h}$	$\frac{d_p-d_m}{h}$	$\frac{\Delta P}{L}$ (Pa/m)	d_p (mm)	μ_g [kg/(m s)]	N_p	$\frac{L}{d_p}$	Re
0.2	500	12.2	1.1	390.6	1.6	1×10^{-5}	108	6.56	172 ± 5
	500	11.9	1.1	390.6	1.6	1×10^{-5}	256	8.75	182 ± 2
	500	12.1	1.1	390.6	1.6	1×10^{-5}	500	10.9	185 ± 2
	500	12.1	1.1	390.6	3.2	2×10^{-5}	256	8.75	181 ± 3
0.4	500	12.1	1.4	2401	1.6	1×10^{-5}	108	5.21	100 ± 10
	500	11.9	1.4	2401	1.6	1×10^{-5}	256	6.95	110 ± 8
	500	12.0	1.4	2401	1.6	1×10^{-5}	500	8.68	112 ± 5

sphere Monte-Carlo procedure can only be used to create configurations with a good randomness at $\phi \leq 0.45$. The randomness depends on detailed parameters like the displacement distance and the number of iterations. In addition, different from simulations of stationary assemblies, we did not observe any obvious influence of the initial configurations on the simulation results of the averaged drag force in dynamic gas-solid suspensions. A steady flow is established by imposing a mean pressure gradient (or body force) over the computational domain, whereas the particles can freely move according to the forces acting on them due to the fluid motion and mutual collisions. Perfectly elastic particle collisions are considered in this work. In such simulations, the mean particle velocity and the mean fluid velocity change in time, but their difference—the mean slip velocity—attains a steady value. This steady-state solution implies a steady value of the mean flow Reynolds number, which depends on the problem parameters (pressure gradient, fluid and particle densities, solids volume fraction, and the particle acceleration), and this value is not known *a priori*. In this work, we specify the pressure gradient for a desired Reynolds number based on the *static* drag correlation reported in Tang et al.[32] Consequently, the obtained steady-state mean *Re* will not equal the desired value, but will be quite close to it.

Domain size

An unbounded suspension is approximated by a suspension consisting of many particles in a cubic unit cell with periodic boundary conditions. We need to first ensure that the computational domain size is sufficiently large so that further increase in box size has a negligible effect on the mean flow quantities. To this end, we have chosen two systems (ϕ=0.2 and 0.4) to investigate the domain size effect, with the parameters listed in Table 2. Particularly for ϕ=0.2 with a domain size of $8.75d_p$, two sets of particle diameter and fluid viscosity are considered while the desired Reynolds number is kept the same. The particle-particle collisions are treated as perfectly elastic through a hard-sphere approach. The simulation results for the mean superficial velocity U and the square root of the mean granular temperature $\sqrt{\Theta}$ are shown in Figure 3a, b for ϕ=0.2 and ϕ=0.4, respectively. The particle granular temperature Θ is evaluated as

$$\Theta=(\Theta_x+\Theta_y+\Theta_z)/3 \tag{19}$$

$$\Theta_k=\frac{1}{N_p}\sum_{n=1}^{N_p}[v_{n,k}(t)]^2-\langle v_k(t)\rangle^2 \qquad k=x,y,z \tag{20}$$

with the mean solids velocity given by

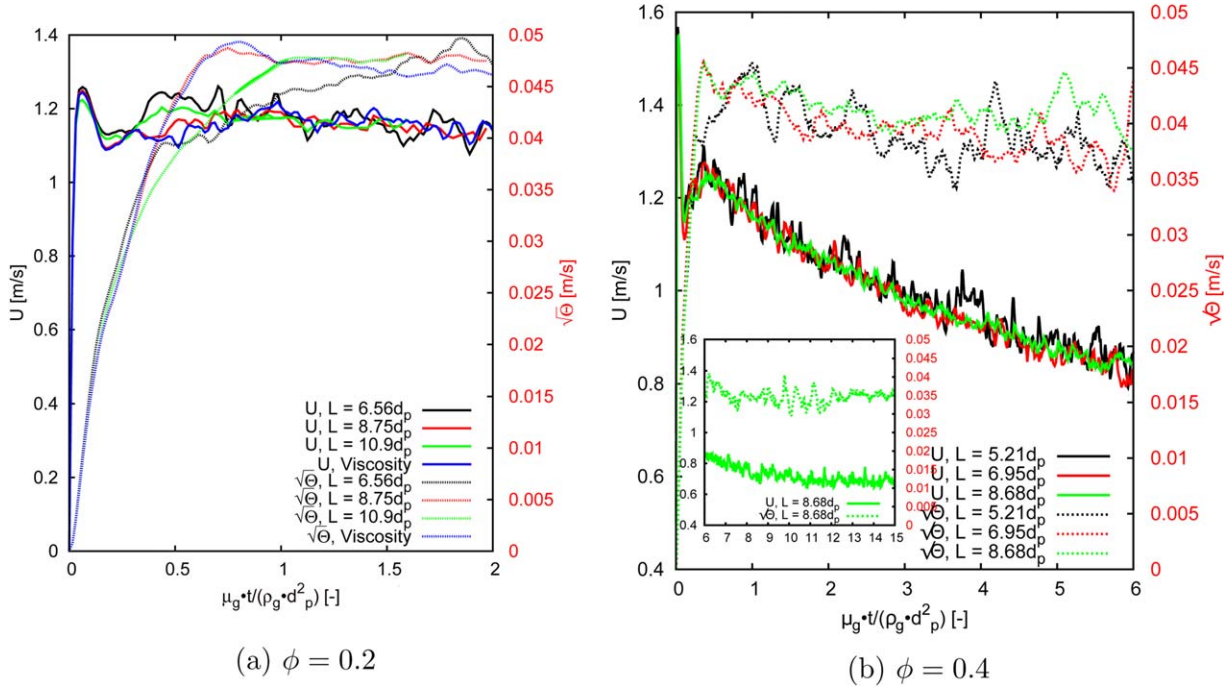

(a) $\phi = 0.2$ (b) $\phi = 0.4$

Figure 3. The mean superficial velocity and the square root of the mean granular temperature from simulations with different domain sizes or viscosity.

(a) ϕ=0.2; (b) ϕ=0.4, only the simulation with $L = 8.68d_p$ was run for a longer time till a steady state was reached, the results of which are plotted in the small window. [Color figure can be viewed in the online issue, which is available at wileyonlinelibrary.com.]

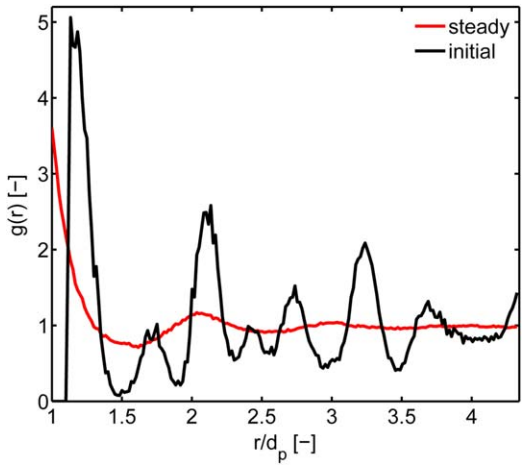

Figure 4. Radial distribution function of particle configurations from simulations of dynamic particles at ϕ=0.4.

The black line is for an initial configuration, while the red line represents the configuration after a steady state is reached in the simulations. [Color figure can be viewed in the online issue, which is available at wileyonlinelibrary.com.]

$$\langle \mathrm{v}_k(t)\rangle = \frac{1}{N_\mathrm{p}}\sum_{n=1}^{N_\mathrm{p}} \mathrm{v}_{n,k}(t) \tag{21}$$

Note that in most of this article, we report the square root of the granular temperature $\sqrt{\Theta}$, in other words the RMS deviation of the particle velocity. Whereas, the mean superficial velocity is evaluated as

$$U = (1-\phi)\,|\langle \mathbf{u}(t)\rangle - \langle \mathbf{v}(t)\rangle| \tag{22}$$

where the mean fluid velocity is given by

$$\langle \mathbf{u}(t)\rangle = \frac{1}{n_x n_y n_z}\sum_{i=1}^{n_x}\sum_{j=1}^{n_y}\sum_{k=1}^{n_z} \mathbf{u}_{i,j,k}(t) \tag{23}$$

with n_x, n_y, n_z the number of computational cells occupied by the gas phase in the respective co-ordinate directions.

First, it can be seen in Figure 3 that the mean superficial velocity and the mean granular temperature both eventually attain a steady value for all the cases considered.* The same observation has been reported by Tenneti et al.[39] that a steady granular temperature is attained not only in the Stokes flow limit but also at moderate Reynolds numbers, which is independent of the initial granular temperature of the suspension. Subsequently, one can observe that from the smallest domain with $N_\mathrm{p} = 108$, which we have utilized for simulations of stationary particles in Tang et al.,[32] a further increase in the domain size has only small influence on U and $\sqrt{\Theta}$. For a fixed Reynolds number and solids volume fraction, variation of particle diameter and fluid viscosity has no influence on the mean flow quantities at the steady state. The same observations have also been found at other solids volume fractions and Reynolds numbers. In addition, it is observed that simulations at ϕ=0.4 take much longer time to reach a steady state than those at ϕ=0.2. The same phenomenon has also been observed for simulations at different Reynolds numbers. From all the simulations (initialized from a rest state) performed in this work, a general observation is that the evolving time to a steady state of a dynamic gas-solid suspension increases with increasing Reynolds number and solids volume fraction.

Figure 4 shows the radial distribution function $g(r)$ of particle configurations originating from simulations of dynamic particles at ϕ=0.4. In this case, some face-centered-cubic structures are locally remained in the initial particle configuration created by the hard-sphere Monte-Carlo procedure. The radial distribution function of this initial configuration is represented by the black line in this figure. Whereas, the red line represents the $g(r)$ computed by averaging over different instantaneous configurations obtained in the simulation after U and $\sqrt{\Theta}$ both reach a statistically steady state. It can be seen that the structure present in the initial configurations have disappeared with a homogeneous particle system prevailing at steady state. We have also confirmed this by visualizing the particle configurations from simulations, which show no obvious particle clustering or structuring at steady state. Such a homogeneous state, independent of the randomness of the initial configurations, has been observed or all the simulations of dynamic suspensions reported in this article.

Simulations of dynamic particles

IBM simulations of dynamic particles have been performed for various solids volume fractions, Reynolds numbers, as well as different particle/gas density ratios. The general simulation parameters are listed in Table 3. As evident from Figure 3, the domain size has a minor effect on the mean flow quantities, thus we have kept a computational domain size of about $10d_\mathrm{p}$ for all the simulations conducted for prediction of the drag force. Besides, the optimal d_m for marker points distribution is evaluated individually in terms of d_p/h, ϕ, and the estimated Re corresponding to the specified pressure gradient. All the simulations were continued such that both the granular temperature and the superficial velocity reached their steady-state values. Time-averaging of U, Θ, and dimensionless drag force F_d (drag force normalized by the Stokes drag) was subsequently performed.

Granular Temperature. Figure 5 shows the evolution of the granular temperature with respect to its three components (x-, y- and z-directions) from simulations of dynamic particle suspensions at solids volume fractions of 0.2 and 0.4, respectively. It can be seen that initially Θ_z is significantly larger than the other two components of the granular temperature,

Table 3. Parameters used for Simulations of Dynamic Particles

Parameters	Values	Units
Particle density ρ_p	[500, 3000]	kg/m^3
Particle diameter d_p	1.6×10^{-3}	m
Domain size L	$\sim 10d_\mathrm{p}$	m
Gas density ρ_g	1	kg/m^3
Gas viscosity μ_g	1×10^{-5}	kg/(m s)
Grid resolution d_p/h	$\sim$12	–
Reynolds number Re	(40, 1000)	–
Solids volume fraction ϕ	[0.1, 0.45]	–
Normal restitution coefficient	1	–
Tangential restitution coefficient	1	–
Friction coefficient	0	–
Time step	$[1\times10^{-6}, 1\times10^{-7}]$	s

*No obvious influence of the domain size on the results was observed from these simulations at ϕ=0.4 shown in Figure 3b. Thus, only the simulation with $L = 8.68d_\mathrm{p}$ was run for a longer time till a steady state was reached. The results of the mean superficial velocity and the square root of the granular temperature from this extended simulation are shown in the small box inside Figure 3b.

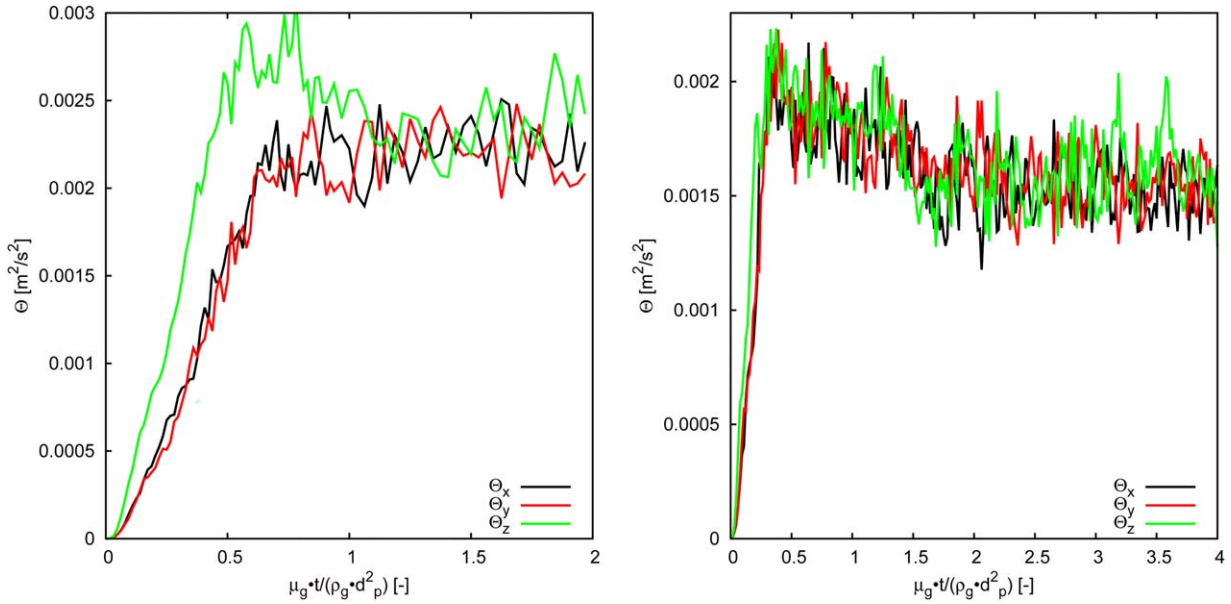

Figure 5. Three components of the granular temperature as a function of dimensionless time from simulations of dynamic particles at ϕ=0.2 (left) and ϕ=0.4 (right).

[Color figure can be viewed in the online issue, which is available at wileyonlinelibrary.com.]

which can be attributed to the body force acting in the z-direction. Nevertheless, it becomes isotropic when the steady state is reached. Such an isotropic granular temperature is expected, since perfectly elastic collisions of particles are assumed in the present simulations.

As evident from Figure 4, the evolving gas-solid suspensions are homogeneous at a steady state regardless of the initial particle configurations. In statistically homogeneous suspensions with elastic particle-particle collisions, the particle acceleration-velocity covariance alone governs the evolution of the granular temperature. Fluctuations in the hydrodynamic force experienced by particles in a gas-solid flow affect the evolution of particle velocity fluctuations, which in turn can affect the mean and variance of the hydrodynamic force. Therefore, it is significant to evaluate the particle velocity fluctuations (or granular temperature) for the development of an accurate expression for the drag law. To quantify the magnitude of particle velocity fluctuations in terms of dimensionless parameters, we define a Reynolds number Re_T based on the granular temperature as

$$Re_T = \frac{\rho_g d_p \sqrt{\Theta}}{\mu_g} \tag{24}$$

Figure 6a shows the data of steady Re_T obtained from IBM simulations at different solids volume fractions and Reynolds numbers for a particle/gas density ratio of 500. It is observed that the steady granular temperature varies only slightly with

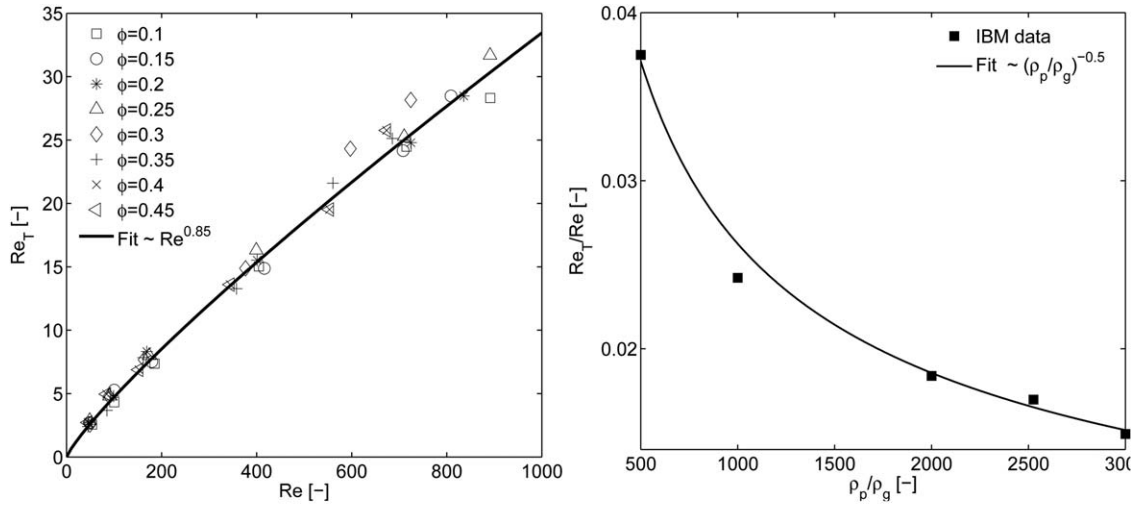

Figure 6. Symbols in (a) represent simulation data of steady Re_T at different solids volume fractions and Reynolds numbers for a density ratio of 500, whereas the solid line indicates the fit given by Eq. 25. (b) shows the variation of steady Re_T normalized by Re with particle/gas density ratio for ϕ=0.4 and $Re = 450 \pm 40$.

Symbols denote the data from IBM simulations and the solid line indicates the function $(\rho_p/\rho_g)^{-0.5}$ as in Eq. 25.

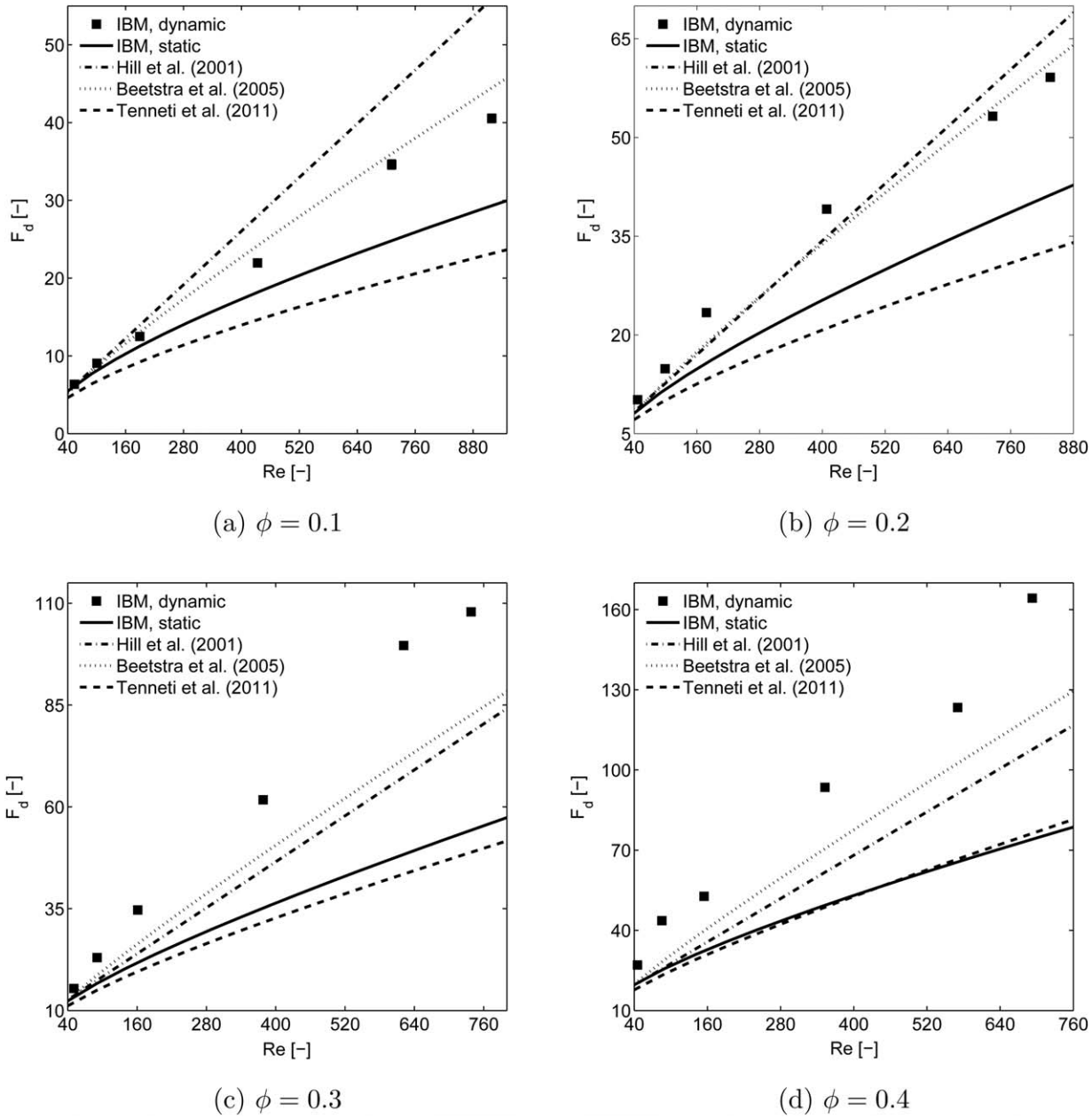

Figure 7. Dimensionless drag force as a function of mean flow Reynolds number at different solids volume fractions.

The symbols represent the data obtained from IBM simulations of dynamic particles with a particle/gas density ratio of 500. Note that the error bars are too small to visualize. The lines indicate the drag correlations developed based on DNS of stationary particles; solid lines for Tang et al.,[32] dash-dot lines for Hill et al.,[28] dotted lines for Beetstra et al.,[30] and dashed lines for Tenneti et al.[31]

the solids volume fraction, but significantly increases with the mean flow Reynolds number. This observation can be explained based on the fact that the particles pick up energy from the gas phase where the energy in the system increases with increasing Re. Figure 6b shows the variation of the steady Re_T with particle/gas density ratio for a solids volume fraction of 0.4. The steady Re_T is normalized by the steady flow Re, which for the data points considered in this figure is about 450 ± 40 as it is not known *a priori*. It is found that the steady granular temperature decreases with increasing density ratio. This observation is expected because particle velocities change slowly due to higher inertia of the particle (larger density ratio). A similar dependence of the steady granular temperature on mean flow Reynolds number and particle/gas density ratio has also been reported by Tenneti et al.[39] Finally based on all the data obtained from our IBM simulations, the following function is proposed for Re_T based on the steady granular temperature

$$Re_T\left(Re, \frac{\rho_p}{\rho_g}\right) = 2.108 Re^{0.85}\left(\frac{\rho_p}{\rho_g}\right)^{-0.5} \tag{25}$$

which gives an average relative deviation of 5.5% compared to the basic simulation data. The fitted curves shown in Figure 6 indicate that the agreement is quite satisfying. We stress that this expression is best to apply for dynamic gas-solid

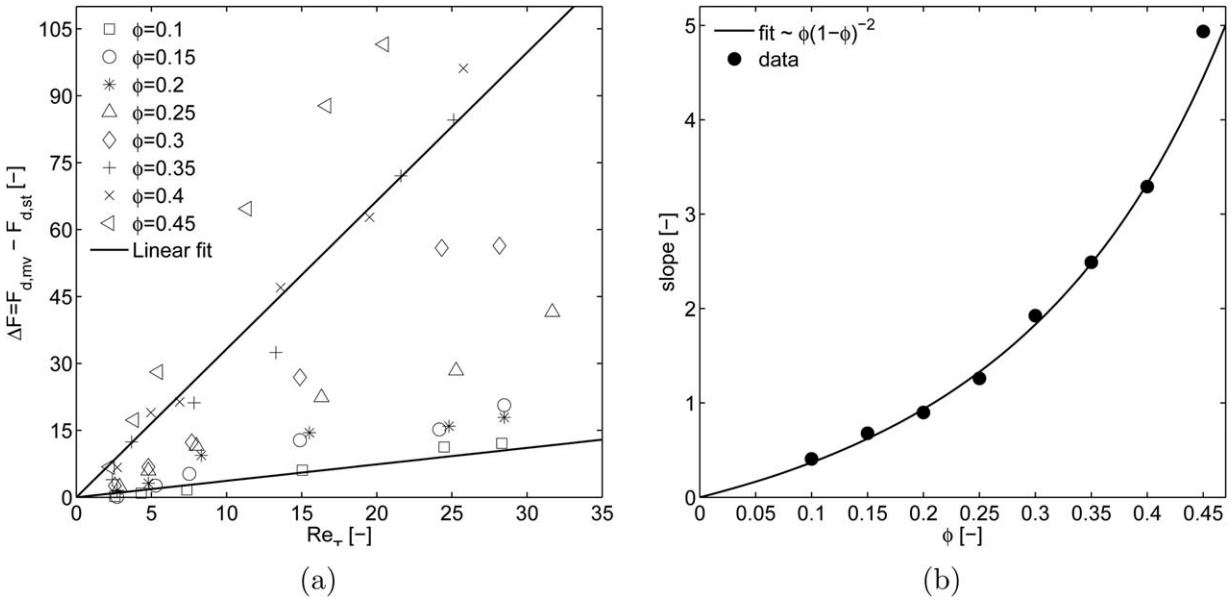

Figure 8. Deviation of the dimensionless drag force ΔF between dynamic particles ($\rho_p/\rho_g = 500$) and stationary particles obtained from IBM simulations.

$F_{d,st}$ is obtained from the correlation in Tang et al.[32] with the corresponding values of Re and ϕ for the simulation data of *dynamic* drag force $F_{d,mv}$. (a) Shows variations of ΔF as a function of Re_T at different solids volume fractions. (b) Plot of the slope shows variations of $\Delta F/Re_T$ as a function of ϕ. The solid lines represent sample fits given by Eq. 26.

suspensions with elastic particle collisions. At given ϕ, ρ_p/ρ_g and Re, inelastic collisions along with energy dissipation may result in a decrease in the magnitude of the granular temperature.

A new (dynamic) drag correlation

Simulation data of Re, Re_T, and dimensionless drag force F_d have been obtained from IBM simulations of dynamic particles for different flow systems with a particle/gas density ratio of 500. All these values are calculated by time-averaging over the simulation results after a steady state has been reached. Figure 7 compares the simulation data of F_d for dynamic particles with some drag correlations developed on the basis of DNSs of stationary particles. The symbols denote the simulation data for Reynolds numbers covering a range from 40 to 900 and solids volume fractions of 0.1, 0.2, 0.3, and 0.4, respectively. The solid lines represent the *static* drag correlation derived from our IBM simulations of flows past random arrays of stationary particles detailed in Tang et al.[32] By direct comparison of our simulation results for dynamic suspensions and static arrays, it is clear that the drag force is enhanced due to the particle mobility. With fixed solids properties, this enhancement of the drag force increases with both Reynolds number and solids volume fraction. In addition, the *static* drag correlations proposed by Hill et al.,[28] Beetstra et al.[30] and Tenneti et al.[31] are also plotted in Figure 7 by dash-dot lines, dotted lines and dashed lines, respectively. Clearly, the drag force predicted by the correlation of Tenneti et al.[31] is smaller than the *dynamic* drag force at arbitrary Re and ϕ. In contrast, the correlations of Hill et al.[28] and Beetstra et al.[30] produce a *static* drag force that exceeds the *dynamic* drag at small solids volume fractions and high Reynolds numbers. Conversely, the *dynamic* drag forces at larger ϕ or small Re are still larger than those given by these two correlations. Such observations can be expected based on the features of these correlations, which were analyzed in detail in Tang et al.[32] Generally speaking, owing to the relatively low resolutions for the conducted LBM simulations, both the correlations of Hill et al.[28] and Beetstra et al.[30] overpredict the drag force for stationary particles, which coincidentally makes them to approach the true drag law for dynamic particle systems. This conclusion also explains the fairly successful application of these two correlations in DEM and TFM simulations of gas-solid flows.

The contribution of the particle mobility to the gas-solid interactions can be directly quantified by comparing our simulation results of the drag force for dynamic particles to those for stationary particles at otherwise identical conditions. Figure 8a shows the behavior of the force deviation ΔF, which is the *dynamic* drag subtracted by the *static* drag, as a function of Re_T for different solids volume fractions. It is found that at a given ϕ, ΔF increases linearly with Re_T, which can be anticipated by the sample fits shown in this figure. The slope of this linear fit varies with ϕ, and is further observed to be proportional to $\phi(1-\phi)^{-2}$ as shown in Figure 8b. Finally the following relation is obtained

$$\Delta F = 2.98 Re_T \frac{\phi}{(1-\phi)^2} \tag{26}$$

which quantifies the contribution of the particle velocity fluctuations to the drag force. Together with the characteristics of Re_T expressed by Eq. 25, it is understood that for dynamic particles the gas-solid interaction force increases with Re and ϕ, but decreases with increasing density ratio as well as energy dissipation by inelastic collisions.

Subsequently by introducing Eq. 26 into the *static* drag correlation in Tang et al.,[32] a correlation for the dimensionless drag force in dynamic particle suspensions is obtained as follows

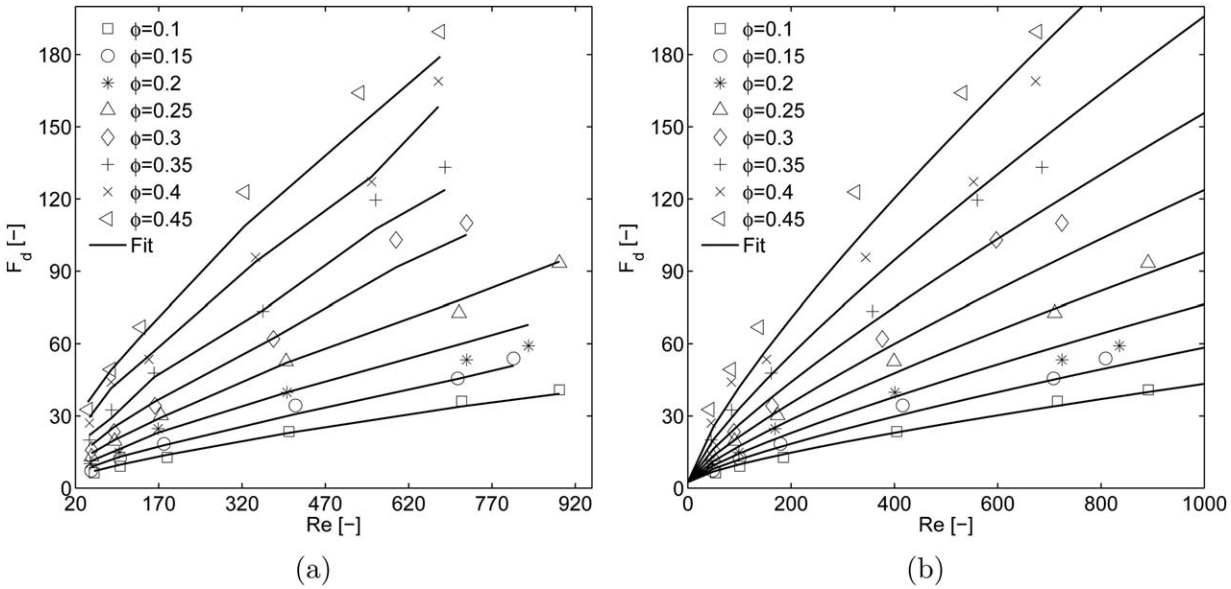

Figure 9. Dimensionless drag force for dynamic particles as a function of *Re* at different solids volume fractions.

Symbols represent the data obtained from IBM simulations. Solid lines in (a) indicate the fits given by Eq. 27, whereas those in (b) represent for Eq. 27 combined with Eq. 25.

$$F_{\mathrm{d}}(\phi,Re,Re_{\mathrm{T}})=\frac{10\phi}{(1-\phi)^2}+(1-\phi)^2(1+1.5\sqrt{\phi})+\left[0.11\phi(1+\phi)-\frac{0.00456}{(1-\phi)^4}+\left(0.169(1-\phi)+\frac{0.0644}{(1-\phi)^4}\right)Re^{-0.343}\right]Re+2.98Re_{\mathrm{T}}\frac{\phi}{(1-\phi)^2} \tag{27}$$

where, the first term is the expression for the drag force at low *Re*, the second term accounts for the inertial effects, whereas the last term represents the particle mobility effect. As shown in Figure 9a, this correlation gives a good fit to our simulation data with an average relative deviation of $|F_{\mathrm{d}}^{\mathrm{sim}}-F_{\mathrm{d}}|/F_{\mathrm{d}}^{\mathrm{sim}}=6.5\%$. So far, Eq. 27 is the first drag correlation established from detailed DNSs of gas-solid flows with mobile particles. With careful investigation of the particle mobility effect on the hydrodynamics, naturally this new *dynamic* drag correlation can replace all the existing correlations for a more detailed description of the effective gas-solid momentum transfer rate in predictive unresolved CFD simulations. Besides, one can combine Eq. 27 with Eq. 25 for a direct estimate of the drag force based on *Re* and ϕ. As shown in Figure 9b, this combination also matches the simulation data quite well, but slightly less accurate than Eq. 27 alone. This can be attributed to the fact that the dependence of Re_{T} on ϕ is not considered in the expression Eq. 25, which as shown in Figure 6a is very weak but does exist. Moreover, Eq. 25 predicts Re_{T} for gas-solid suspensions with elastic collisions, where the energy dissipation due to inelastic collisions is not accounted for. Conversely, at arbitrary particle properties the local granular temperature can be easily calculated in large-scale models such as DEM and TFM via particle individual velocities and KTGF model, respectively. Thus, Eq. 27 can be readily implemented into large-scale predictive CFD models for more accurate prediction of the effective drag force.

Conclusions

In this study, the effect of particle mobility on the gas-solid interaction force has been reported. Simulations have been performed for flows past dynamic suspensions of monodisperse spherical particles using the IBM, while applying the optimal d_m based on the methodology detailed in Tang et al.[45] Using periodic boundary conditions, the domain size for the computational box is found to have a minor effect on the mean flow quantities. Utilizing a domain size of about $10d_{\mathrm{p}}$, we have performed simulations of dynamic particles for various solids volume fractions, Reynolds number, and particle/gas density ratios. For all the simulations, a steady state of *Re*, granular temperature Θ and drag force has been attained, concurrent with a homogeneous suspension which is independent of the initial particle configuration.

First, we have investigated the evolution of the granular temperature, a key parameter characterizing the dynamics of particle suspensions. A modified Reynolds number Re_{T} is defined where the square root of the granular temperature, quantifying the magnitude of the particle velocity fluctuations, is used as the characteristic velocity. It is found that the steady granular temperature varies slightly with ϕ, but increases strongly with increasing *Re* and decreasing particle/gas density ratio. Based on the simulation data for dynamic particles subject to elastic collisions, an expression for Re_{T} is proposed as Eq. 25 in terms of mean flow Reynolds number and density ratio.

Subsequently, the dimensionless drag forces obtained from IBM simulations of dynamic particles are analyzed and compared with several drag correlations that were obtained earlier from DNS of stationary particles. Significant differences have been observed between the *dynamic* drag force and the prediction given by any of the correlations for static arrays. A direct comparison between the data obtained in this work and the results reported in Tang et al.[32] for static particle arrays reveals that the drag force increases due to the particle mobility. The increase in the drag force is further found to possess a linear relation with Re_{T} where the slope varies with ϕ, as

given by Eq. 26. Finally, a new drag correlation Eq. 27 is obtained, for the first time, taking into account the particle mobility effect based on detailed DNS of gas-solid flows. This correlation can be considered so-far the most detailed representation of the effective drag force in unresolved CFD simulations of gas-solid flows.

Acknowledgments

The authors would like to thank the European Research Council for its financial support, under its Advanced Investigator Grant scheme, contract number 247298 (Multiscale Flows).

Literature Cited

1. Anderson TB, Jackson R. Fluid mechanical description of fluidized beds: equations of motion. *Ind Eng Chem Fundam*. 1967;6(4):527–539.
2. Gidaspow D. *Multiphase Flow and Fluidization: Continuum and Kinetic Theory Descriptions*. San Diego, California: Academic Press, 1994.
3. Panneerselvam R, Savithri S, Surender GD. CFD simulation of hydrodynamics of gas-liquid-solid fluidised bed reactor. *Chem Eng Sci*. 2009;64(6):1119–1135.
4. Xiong Q, Deng L, Wang W, Ge W. SPH method for two-fluid modeling of particle-fluid fluidization. *Chem Eng Sci*. 2011;66(9):1859–1865.
5. Verma V, Deen NG, Padding JT, Kuipers JAM. Two-fluid modeling of three-dimensional cylindrical gas-solid fluidized beds using the kinetic theory of granular flow. *Chem Eng Sci*. 2013;102:227–245.
6. Oevermann M, Gerber S, Behrendt F. Euler-Lagrange/DEM simulation of wood gasification in a bubbling fluidized bed reactor. *Particuology*. 2009;7(4):307–316.
7. de Jong JF, van Sint Annaland M, Kuipers JAM. Membrane-assisted fluidized beds-part 1: development of an immersed boundary discrete particle model. *Chem Eng Sci*. 2012;84:814–821.
8. Guo Y, Wu CY, Thornton C. Modeling gas-particle two-phase flows with complex and moving boundaries using DEM-CFD with an immersed boundary method. *AIChE J*. 2013;59(4):1075–1087.
9. Dietiker JF, Li T, Garg R, Shahnam M. Cartesian grid simulations of gas-solids flow systems with complex geometry. *Powder Technol*. 2013;235:696–705.
10. Tsuji T, Higashida K, Okuyama Y, Tanaka T. Fictitious particle method: a numerical model for flows including dense solids with large size difference. *AIChE J*. 2014;60(5):1606–1620.
11. Chesshire G, Henshaw WD. Composite overlapping meshes for the solution of partial differential equations. *J Comput Phys*. 1990;90(1):1–64.
12. Bagchi P, Ha MY, Balachandar S. Direct numerical simulation of flow and heat transfer from a sphere in a uniform cross-flow. *J Fluids Eng*. 2001;123(2):347–358.
13. Hu H, Patankar NA, Zhu MY. Direct numerical simulations of fluid-solid systems using the arbitrary Lagrangian-Eulerian technique. *J Comput Phys*. 2001;169(2):427–462.
14. Henshaw WD, Schwendeman DW. An adaptive numerical scheme for high-speed reactive flow on overlapping grids. *J Comput Phys*. 2003;191(2):420–447.
15. Burton TM, Eaton JK. Fully resolved simulations of particle-turbulence interaction. *J Fluid Mech*. 2005;545:67–111.
16. Peskin CS. Numerical analysis of blood flow in the heart. *J Comput Phys*. 1977;25(3):220–252.
17. Fadlun EA, Verzicco R, Orlandi P, Mohd-Yusof J. Combined immersed-boundary finite-difference methods for three-dimensional complex flow simulations. *J Comput Phys*. 2000;161(1):35–60.
18. Uhlmann M. An immersed boundary method with direct forcing for the simulation of particulate flows. *J Comput Phys*. 2005;209(2):448–476.
19. Ladd AJC. Numerical simulations of particulate suspensions via a discretized Boltzmann equation. Part 1. Theoretical foundation. *J Fluid Mech*. 1994;271:285–309.
20. Glowinski R, Pan TW, Hesla TI, Joseph DD, Priaux J. A fictitious domain approach to the direct numerical simulation of incompressible viscous flow past moving rigid bodies: application to particulate flow. *J Comput Phys*. 2001;169(2):363–426.
21. Prosperetti A, Ogũz HN. Physalis: a new o(N) method for the numerical simulation of disperse systems: potential flow of spheres. *J Comput Phys*. 2001;167(1):196–216.
22. Garg R. Modeling and simulation of two-phase flows. Ph.D. thesis, Iowa State University, Ames, 2009.
23. Breugem WP. A second-order accurate immersed boundary method for fully resolved simulations of particle-laden flows. *J Comput Phys*. 2012;231(13):4469–4498.
24. Tenneti S, Subramaniam S. Particle-resolved direct numerical simulation for gas-solid flow model development. *Ann Rev Fluid Mech*. 2014;46(1):199–230.
25. Prosperetti A, Tryggvason G. *Computational Methods for Multiphase Flow*. Cambridge, UK: Cambridge University Press, 2007.
26. Deen NG, Peters EAJF, Padding JT, Kuipers JAM. Review of direct numerical simulation of fluid-particle mass, momentum and heat transfer in dense gas-solid flows. *Chem Eng Sci*. 2014;116:710–724.
27. Hill RJ, Koch DL, Ladd AJC. The first effects of fluid inertia on flows in ordered and random arrays of spheres. *J Fluid Mech*. 2001;448:213–241.
28. Hill RJ, Koch DL, Ladd AJC. Moderate-Reynolds-number flows in ordered and random arrays of spheres. *J Fluid Mech*. 2001;448:243–278.
29. van der Hoef MA, Beetstra R, Kuipers JAM. Lattice-Boltzmann simulations of low-Reynolds-number flow past mono- and bidisperse arrays of spheres: results for the permeability and drag force. *J Fluid Mech*. 2005;528:233–254.
30. Beetstra R, van der Hoef MA, Kuipers JAM. Drag force of intermediate Reynolds number flow past mono- and bidisperse arrays of spheres. *AIChE J*. 2007;53(2):489–501.
31. Tenneti S, Garg R, Subramaniam S. Drag law for monodisperse gas-solid systems using particle-resolved direct numerical simulation of flow past fixed assemblies of spheres. *Int. J. Multiphase Flow*. 2011;37(9):1072–1092.
32. Tang Y, Kriebitzsch SHL, Peters EAJF, van der Hoef MA, Kuipers JAM. A new drag correlation from fully resolved simulations of flow past monodisperse static arrays of spheres. *AIChE J*. 2015;61(2):688–698.
33. Yin X, Koch DL. Hindered settling velocity and microstructure in suspensions of solid spheres with moderate Reynolds numbers. *Phys Fluids (1994-present)*. 2007;19(9):093302.
34. Wang Z, Fan J, Luo K. Combined multi-direct forcing and immersed boundary method for simulating flows with moving particles. *Int J Multiphase Flow*. 2008;34(3):283–302.
35. Breugem WP. A combined soft-sphere collision/immersed boundary method for resolved simulations of particulate flows. In: *ASME 2010 3rd Joint US-European Fluids Engineering Summer Meeting collocated with 8th International Conference on Nanochannels, Microchannels, and Minichannels*. Montreal, Quebec, Canada: American Society of Mechanical Engineers, 2010, doi:10.1115/FEDSM-ICNMM2010-30634.
36. Yacoubi AE, Sheng X, Wang ZJ. Computational study of the interaction of freely moving particles at intermediate Reynolds numbers. *J Fluid Mech*. 2012;705:134–148.
37. Shardt O, Derksen JJ. Direct simulations of dense suspensions of non-spherical particles. *Int J Multiphase Flow*. 2012;47:25–36.
38. Wylie JJ, Koch DL, Ladd AJC. Rheology of suspensions with high particle inertia and moderate fluid inertia. *J Fluid Mech*. 2003;480(10):95–118.
39. Tenneti S, Garg R, Hrenya CM, Fox RO, Subramaniam S. Direct numerical simulation of gassolid suspensions at moderate Reynolds number: quantifying the coupling between hydrodynamic forces and particle velocity fluctuations. *Powder Technol*. 2010;203(1):57–69.
40. Yin X, Sundaresan S. Fluid-particle drag in low-Reynolds-number polydisperse gassolid suspensions. *AIChE J*. 2009;55(6):1352–1368.
41. Kriebitzsch SHL, van der Hoef MA, Kuipers JAM. Fully resolved simulation of a gas-fluidized bed: a critical test of DEM models. *Chem Eng Sci*. 2013;91:1–4.
42. Centrella J, Wilson JR. Planar numerical cosmology. II-The difference equations and numerical tests. *Astrophys J Suppl Ser*. 1984;54:229–249.
43. Deen NG, van Sint Annaland M, Kuipers JAM. Multi-scale modeling of dispersed gas-liquid two-phase flow. *Chem Eng Sci*. 2004;59(8–9):1853–1861.
44. Hoomans BPB, Kuipers JAM, Briels WJ, van Swaaij WPM. Discrete particle simulation of bubble and slug formation in a two-dimensional gas-fluidised bed: a hard-sphere approach. *Chem Eng Sci*. 1996;51(1):99–118.
45. Tang Y, Kriebitzsch SHL, Peters EAJF, van der Hoef MA, Kuipers JAM. A methodology for highly accurate results of direct numerical

simulations: drag force in dense gassolid flows at intermediate Reynolds number. *Int J Multiphase Flow*. 2014;62:73–86.
46. Kriebitzsch SHL. Direct numerical simulation of dense gas-solid flows. Ph.D. Thesis, Eindhoven University of Technology, The Netherlands. 2011.
47. ten Cate A, Nieuwstad CH, Derksen JJ, den Akker HEAV. Particle imaging velocimetry experiments and lattice-Boltzmann simulations on a single sphere settling under gravity. *Phys Fluids*. 2002;14(11): 4012–4025.
48. Frenkel D, Smit B. Understanding molecular simulation: from algorithms to applications. *Comput Sci Ser*. 2002;1:1–638.

Manuscript received Aug. 12, 2015, and revision received Jan. 21, 2016.